Theoretical & finite-element analysis of ultrasonic vortex beam generation with single-element transducer & phase plate

Chirag Gokani, Yuqi Meng

Going on means going far
Going far means returning

Tao Te Ching [1]

Abstract

Acoustic vortex beams have a wide range of applications in underwater, biomedical, physical, and engineering acoustics. Studying their physical structure provides new perspectives that may enhance the utility and precision of these applications. As such, the pressure field of a vortex beam generated by a single-element transducer and phase plate is studied from four perspectives: the Rayleigh integral, Fourier acoustics, the Fresnel approximation, and the finite element method (FEM). The Rayleigh integral method replicates the results presented in [2] by Terzi et al. The other three methods facilitate the study of various characteristics of vortex beams. Notably, a semi-analytical solution is found in the near field, and an analytical solution is found in the focal plane.

Section (1) outlines the problem. Section (2) presents the numerical integration of the first and second Rayleigh integrals, replicating [2]. Sections (3) and (4) respectively offer Fourier acoustics and Fresnel limit perspectives. Section (5) presents a finite element analysis. Section (6) suggests how these results can enhance engineering applications of vortex beams. The $e^{-i\omega t}$ convention is used.

1 Outline of the problem

To generate a vortex beam, Terzi et al. impart angular momentum to a propagating pressure wave. The propagating wave is generated by a transducer, and the angular momentum is

Parameter	Description	Value (mm)
z_{00}	transducer depth	13.4
z_{01}	distance from phase plate to outer edge of transducer	10
z_1	distance from center of transducer to phase plate	23.4
z_0	distance from center of transducer to plane of observation	100

Table 1: Positions of elements as reported in [2] measured from $z = 0$ along the z-axis

Parameter	Description	Value	Dimensions
F	surface curvature radius of transducer	100	mm
D	diameter of transducer	100	mm
f	drive frequency of transducer	1.092	MHz
ρ_0	density of water	1000	kg/m^3
c_0	speed of sound in water	1481	m/s

Table 2: Geometric and physical properties of transducer and background medium

imparted by a phase plate. Figure (1) shows the arrangement of these elements, and table (1) provides their positions along the z-axis. Table (2) provides the material properties.

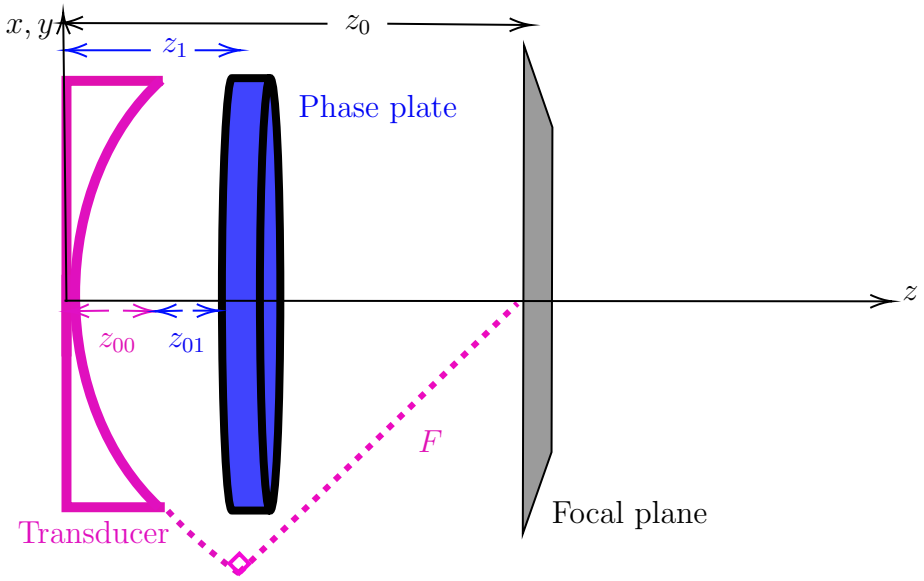

Figure 1: Positions of the transducer, phase plate, and focal plane, respectively denoted by subscripts $_{\mathrm{T}}$, $_1$, and $_0$.

The transducer is spherically focused and pulsates at frequency f (corresponding to wavenumber $k = 2\pi f/c_0$) with normal vibration velocity amplitude V. The surface of the transducer, denoted S_{T}, has differential area $\mathrm{d}S_{\mathrm{T}}$. The distance from a point on

the transducer $(x_\mathrm{T}, y_\mathrm{T}, z_\mathrm{T})$ to a point on the phase plate (x_1, y_1, z_1) is given by $R_\mathrm{T} = \sqrt{(x_1 - x_\mathrm{T})^2 + (y_1 - y_\mathrm{T})^2 + (z_1 - z_\mathrm{T})^2}$, where $z_\mathrm{T} = \frac{2F - \sqrt{4F^2 - 4(x_\mathrm{T}^2 + y_\mathrm{T}^2)}}{2}$ [3].

Meanwhile, the phase plate lies at $z = z_1 = z_{00} + z_{01}$ and contributes vorticity to the pressure field generated by the transducer. The surface of the phase plate, denoted S_1, has differential surface area $\mathrm{d}S_1$. The distance from the phase plate to a point on the focal plane (x_0, y_0, z_0) is given by $R_0 = \sqrt{(x_0 - x_1)^2 + (y_0 - y_1)^2 + (z_0 - z_1)^2}$.

Physically, the vorticity is achieved by varying the phase plate's thickness over the polar angle $\varphi \equiv \arctan(y_1/x_1)$; the incident pressure wave accumulates a local phase depending on the thickness through which it passes. Mathematically, the vorticity contributes a factor of $e^{i\Phi(\varphi)}$ to the complex-exponential form of solution. Since vortex beams are by definition helices that repeat their angular behavior over many cycles in φ, $e^{i\Phi(\varphi)}$ must be either constant or periodic in $2\pi/l$, where l = the orbital number $= \pm 1, \pm 2, \ldots$. That is,

$$\Phi(\varphi) = \begin{cases} 0, & e^{i\Phi(\varphi)} \text{ is constant} \\ l\varphi, \text{ where } l = \pm 1, \pm 2, \ldots, & e^{i\Phi(\varphi)} \text{ is periodic in } 2\pi/l \end{cases}$$

So, $\Phi(\varphi) = l\varphi$ where $l = 0, \pm 1, \pm 2, \ldots$. The $l = 0$ mode has no vorticity, the $l = \pm 1$ mode features one equal-phase surface, and larger values of l correspond to families of l helicoids.

The phase is treated mathematically in sections (2), (3), and (4), and physically in section (5). Following [2], the $l = 3$ orbital number is considered throughout, and $\Phi(\varphi)$ is defined as $\Phi(\varphi) = l\frac{n\pi}{6}$ for $\frac{(n-1)\pi}{6} < \varphi \leqslant \frac{n\pi}{6}$ where $n = 1, 2, \ldots 12$ in sections (2) and (3). To develop an analytical solution, $\Phi(\varphi)$ is defined as $\Phi(\varphi) = l\varphi$ for $0 < \varphi \leqslant 2\pi$, in section (4).

There are two defining characteristics of the vortex beam: (1) its vanishing on-axis pressure magnitude when projected on the transverse plane, and (2) its l-helicoid phase structure. These features guide the discussion in the following sections.

2 Rayleigh integral solution

To calculate the pressure field at the focal plane, the problem is split into two parts. The first part involves calculating the pressure field generated by the transducer at z_1^-, a plane on the z-axis infinitesimally less than z_1. The pressure at this point is $p(x_1, y_1, z_1^-)$ and is given by the first Rayleigh integral [4]:

$$p(x_1, y_1, z_1^-) = -i\frac{\rho_0 c_0 k}{2\pi} \iint_{S_T} \frac{V e^{ikR_T}}{R_T} \, \mathrm{d}S_T \qquad \text{(first Rayleigh integral)}$$

where the variables are as defined in section (1). V can be factored out of the integral because it is constant and can be set to unity since the results are presented in a dimensionless form. The surface S_T is the section of a sphere of radius F tangent to the origin such that the projection of the surface on the $z = 0$ plane has radius 50 mm, as reflected in the definition of R_T [4].

To numerically evaluate the (first Rayleigh integral), a 100 mm $\times$ 100 mm plane at $z = 0$ is discretized using a square mesh with elementary side length $h = \lambda/4.097 = .331$ mm. Figure (2) is the result of this integration as observed from a 75 mm $\times$ 75 mm plane at $z = z_1^-$ discretized using a square mesh of $h = \lambda/2.731 = .497$ mm.

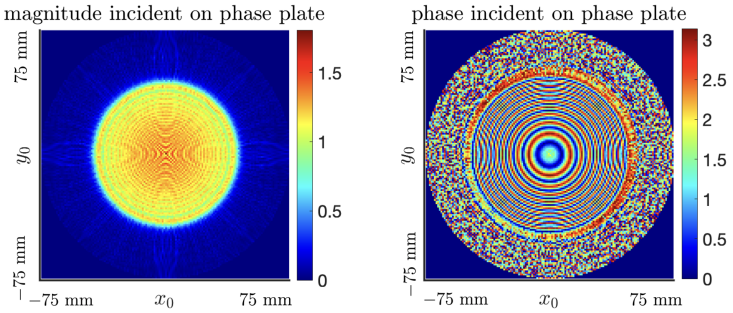

Figure 2: Normalized pressure magnitude $|(p(x_1, y_1, z_1^-)|/\rho_0 c_0 u_0$ (left) and phase $\angle p(x_1, y_1, z_1^-)$ (right) incident on the phase plate

As the pressure wave passes through the phase plate, it accumulates vorticity, so the emerging pressure wave is $p(x_1, y_1, z_1^+) = p(x_1, y_1, z_1^-)e^{3i\varphi}$. The second Rayleigh integral [5] treats $p(x_1, y_1, z_1^+)$ as a pressure source and calculates the pressure field at the focal plane

$z = z_0$:

$$p(x_0, y_0, z_0) = \frac{1}{2\pi} \oiint_{S_1} p(x_1, y_1, z_1^+) \frac{z_0 - z_1}{R_0} \left(-\frac{ik}{R_0} + \frac{1}{R_0^2} \right) e^{ikR_0} \, \mathrm{d}S_1$$

(second Rayleigh integral)

where the variables are as defined in section (1). To numerically evaluate the (second Rayleigh integral), the integral is taken over the 75 mm × 75 mm plane of the phase plate. Figure (3) is the result of this integration at a 5 mm × 5 mm plane at $z = z_0 = F$ discretized using a square mesh of $h = \lambda/40.958 = 0.0331$ mm. The results match those in [2].

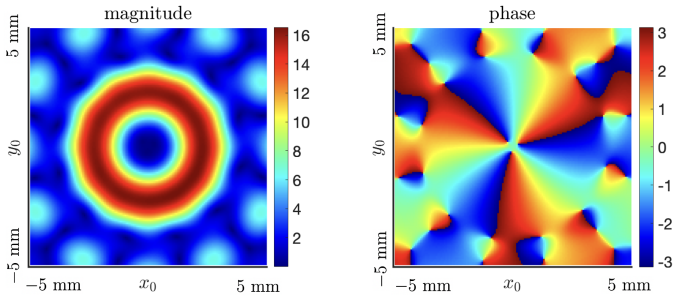

Figure 3: Normalized pressure magnitude $|(p(x_0, y_0, z_0)|/\rho_0 c_0 u_0$ (left) and phase $\angle p(x_0, y_0, z_0)$ (right) at the focal plane. The pressure magnitude vanishes on-axis, and the three helicoids corresponding to $l = 3$ are seen in the phase, confirming vortex-beam behavior.

3 Fourier acoustics solution

Fourier acoustics allows for the efficient computation of the pressure field at intermediate points, allowing for the study of the evolution of the vortex beam along its path to the focal plane. [7] derives equations (1) and (2), and [8] is used to perform the calculations.

The setup summarized in tables (1) and (2) is used, except the transducer now operates at a slightly lower frequency of 1 MHz, the phase plate is positioned at $z_1 = 7.5$ mm, and the plane of observation is set to a closer distance of 12.5 mm. Figure (4) provides a schematic.

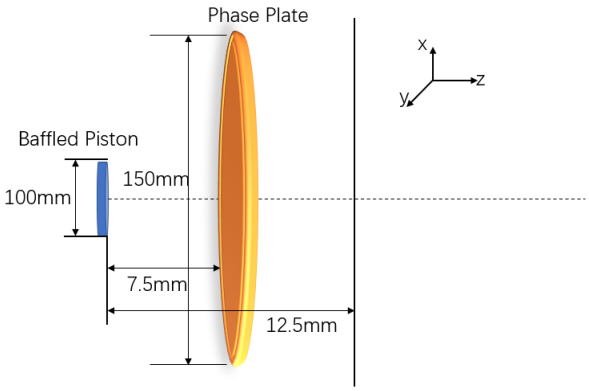

Figure 4: Relative positions of the source, phase plate, and focal plane in the Fourier treatment. This setup differs from that shown in figure (1): since the evolution of the vortex beam from the transducer to a short distance beyond the phase plate is of interest, an observation plane closer than the focal plane is considered, allowing for higher resolution.

The problem is again split into two. First, equation (1) calculates the pressure incident on the phase plate, as shown in figure (5).

$$p(x_1, y_1, z_1) = \rho_0 c_0 F^{-1}\left\{\frac{k}{k_z}\hat{u}_{\mathrm{T}}(k_x, k_y)e^{ik_z z}\right\} \tag{1}$$

Second, a phase factor is included in the field at the phase plate to account for the vorticity. The field is then propagated by inserting the solution from equation (1) into

$$p(x_0, y_0, z_0) = F^{-1}\{F\{p(x_1, y_1, 7.5\text{ mm})e^{3il}\}e^{i\Phi(\varphi)}\}. \tag{2}$$

Figure (6) displays the pressure magnitude and phase immediately after leaving the phase plate, and figure (7) shows the pressure magnitude in the y-z plane in that vicinity. Figure (8) displays the magnitude and phase in the plane $z = 12.5$ mm and demonstrates the defining characteristics of vortex beams. Figure (9) shows the full journey of the vortex beam, from transducer to a plane of observation past the phase plate.

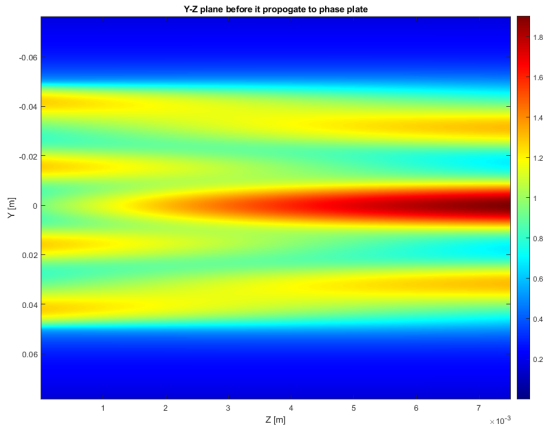

Figure 5: Magnitude of equation (1) normalized by $\rho_0 c_0 u_0$. The on-axis magnitude grows due to spherical focusing of transducer.

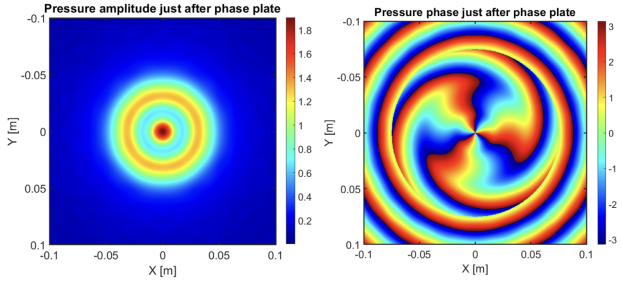

Figure 6: Pressure magnitude (left) and phase (right) shortly after exiting the phase plate. The development of the $l = 3$ phase pattern is seen.

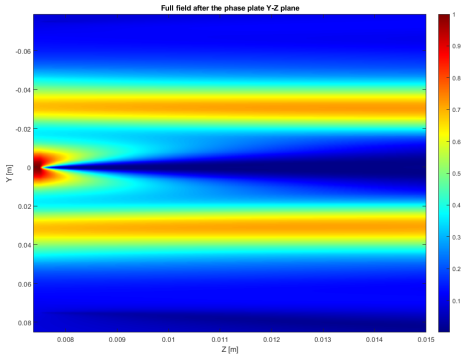

Figure 7: Magnitude of the pressure field in the y-z plane after exiting the phase plate. Destructively interfere on-axis starts at $z = 7.5$ mm and grows conically.

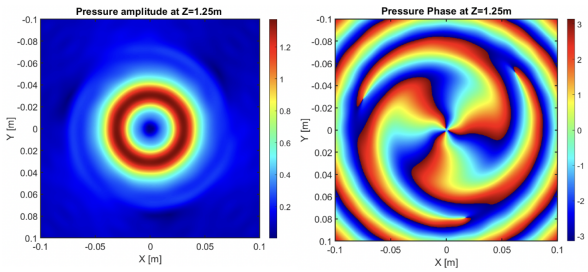

Figure 8: Pressure magnitude (left) and phase (right) at $z = 1.25$ cm. The vanishing on-axis magnitude and $l = 3$ vorticity are well-developed even at this early observation distance.

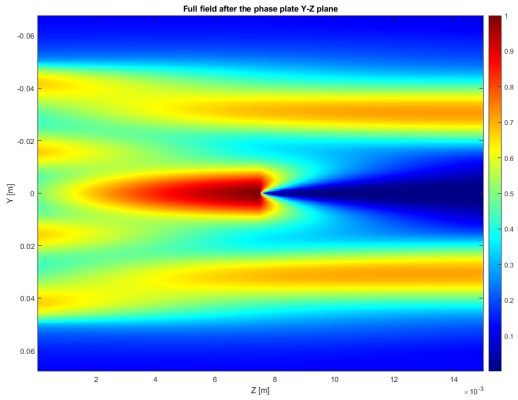

Figure 9: From $z = 0$ to $z = 7.5$ mm, the pressure evolves into an on-axis maximum; from $z = 7.5$ to $z = 12.5$ mm, the vorticity destructively evolves the on-axis amplitude into a null.

4 Fresnel limit

The motivation of exploring the Fresnel limit is twofold. First, to the authors' knowledge, an analytical solution for the vortex beam has not been discussed in the literature. The investigation of the Fresnel limit has grown beyond the scope of the task at hand and is being pursued independently. Second, an approximation of the results can drastically reduce computation time in future work. To these ends, the Fresnel approximation, which gives the pressure at point (x, y, z) in the near field of a velocity source $u_0(x_0, y_0)$, is employed:

$$p(x,y,z) \simeq \frac{-ik\rho_0 c_0}{2\pi}\frac{e^{ikz}}{z}\iint_{-\infty}^{\infty} u_0(x_0,y_0)\exp\Big[\frac{ik}{2z}\left((x-x_0)^2+(x-x_0)^2\right)\Big]\,\mathrm{d}x_0\,\mathrm{d}y_0. \qquad (3)$$

Note that a different notation is used in this section: the '0' subscript now refers to the source. Introducing polar coordinates, $(x,y) = (\sigma\cos\varphi, \sigma\sin\varphi)$, $(x_0,y_0) = (\sigma_0\cos\varphi_0, \sigma_0\sin\varphi_0)$, $\mathrm{d}x_0\,\mathrm{d}y_0 = \sigma_0\,\mathrm{d}\sigma_0\,\mathrm{d}\varphi_0$, where $\sigma = \sqrt{x^2+y^2}$, $\sigma_0^2 = \sqrt{x_0^2+y_0^2}$, $\varphi = \arctan y/x$, and $\varphi_0 = \arctan y_0/x_0$, the argument of the exponential in equation (3) becomes $(x-x_0)^2+(y-y_0)^2 = \sigma^2+\sigma_0^2-2\sigma\sigma_0\cos(\varphi_0+\varphi)$, upon which equation (3) becomes

$$p(\sigma,z,\varphi) = \frac{-ik\rho_0 c_0}{2\pi}\frac{e^{ikz}}{z}e^{ik\sigma^2/2z}\int_0^{\infty} u_0(\sigma_0,\phi_0)\exp\left(\frac{ik}{2z}\sigma_0^2\right)\sigma_0\int_0^{2\pi}\exp\Big[\frac{-ik\sigma\sigma_0}{z}\cos(\varphi_0+\varphi)\Big]\,\mathrm{d}\varphi_0\,\mathrm{d}\sigma_0. \quad (4)$$

The curvature of the transducer contributes a factor of $\exp\left(-ik\sigma_0^2/2F\right)$, while the phase plate contributes a factor of $e^{i\Phi}$, where $\Phi = l\varphi$ for $0 \leqslant \varphi < 2\pi$. Equation (4) becomes

$$\begin{aligned} p(\sigma,z,\varphi) \simeq{}& \frac{-ik\rho_0 c_0}{2\pi}\frac{e^{ikz}}{z}e^{ik\sigma^2/2z}\times \\ &\times\int_0^{\infty} u_0(\sigma_0,\phi_0)\exp\Big[\frac{ik}{2}\left(\frac{1}{z}-\frac{1}{F}\right)\sigma_0^2\Big]\sigma_0\int_0^{2\pi}\exp\Big[\frac{-ik\sigma\sigma_0}{z}\cos(\varphi_0+\varphi)\Big]e^{il\varphi}\,\mathrm{d}\varphi_0\,\mathrm{d}\sigma_0. \end{aligned} \quad (5)$$

The angular integral in equation (5), upon changing variables $\varphi_0+\varphi \mapsto \varphi'$, becomes

$$e^{-il\varphi}\int_0^{2\pi}\exp\Big[\frac{-ik\sigma\sigma_0}{z}\cos\varphi'\Big]e^{il\varphi'}\,\mathrm{d}\varphi'. \qquad (6)$$

The limits of integration remain because cosine is periodic in 2π. Substituting $k\sigma\sigma_0/2 \mapsto \eta$, the integral in (6) renders itself as an integral representation of the Bessel function [11], $\frac{2\pi}{e^{il\pi/2}}J_l(\eta) = \int_0^{2\pi} e^{il\varphi'-i\eta\cos\varphi'}\,\mathrm{d}\varphi'$, upon which (6) becomes

$$\frac{2\pi e^{-il\varphi}}{e^{il\pi/2}} J_l(k\sigma\sigma_0/z). \tag{7}$$

Substituting (7) into equation (5) results in a semi-analytical solution for any l:

$$p(\sigma, z) \simeq \frac{-ik\rho_0 c_0}{e^{il\pi/2}} \frac{e^{ikz}}{z} e^{ik\sigma^2/2z} \times \\ \times \int_0^\infty u_0(\sigma_0, \varphi_0) \exp\left[\frac{ik}{2}\left(\frac{1}{z} - \frac{1}{F}\right)\sigma_0^2\right] J_l(k\sigma\sigma_0/z)\sigma_0 \, \mathrm{d}\sigma_0. \tag{8}$$

For $l = 3$, equation (8) becomes

$$p(\sigma, \varphi, z) \simeq k\rho_0 c_0 u_0 \frac{e^{ikz}}{z} e^{ik\sigma^2/2z} e^{-3i\varphi} \times \\ \times \int_0^a \exp\left[\frac{ik}{2}\left(\frac{1}{z} - \frac{1}{F}\right)\sigma_0^2\right] J_3(k\sigma\sigma_0/z)\sigma_0 \, \mathrm{d}\sigma_0 \tag{9}$$

Moving into the focal plane $z = F$, the semi-analytical solution becomes analytical:

$$p(\sigma, \varphi, F) \simeq \rho_0 c_0 u_0 \frac{F}{k\sigma^2} e^{ikF} e^{ik\sigma^2/2F} e^{3i\varphi} \left[\left(\frac{3\pi}{2}\frac{ka\sigma}{F}\mathbf{H}_0(ka\sigma/F) - 8\right) J_1(ka\sigma/F) + \right. \\ \left. + \left(\frac{4ka\sigma}{F} - \frac{3\pi ka\sigma}{2F}\mathbf{H}_1(ka\sigma/F)\right) J_0(ka\sigma/F) \right] \tag{10}$$

Figure (10) compares the exact Rayleigh solution to equation (10), as well as to the numerical integration of equation (9) at $z = F$. Figures (11) and (13) display the pressure field computed using the Rayleigh and Fresnel solutions, respectively.

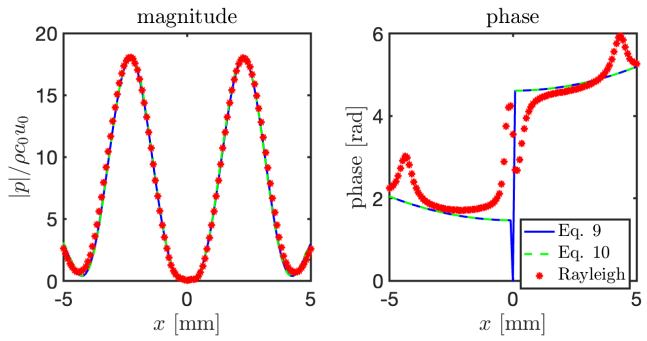

Figure 10: Magnitudes (left) and phases (right) of the exact Rayleigh and Fresnel solutions along the line $y = 0$ in the focal plane for $l = 3$. Equation (9) exactly matches (10), and both closely match the Rayleigh result. The discrepancy near ± 4.75 mm is likely due to the Fresnel approximation's decreasing accuracy off-axis.

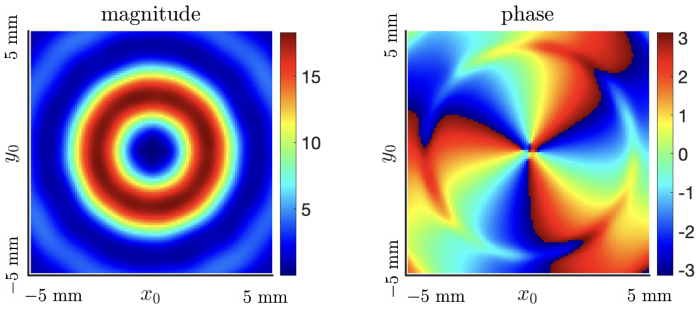

Figure 11: Magnitude (left) and phase (right) of the Rayleigh solutions in the focal plane for $l = 3$. The same parameters and normalization used to generate figure (3) were used here, except that the phase plate imparts a continuous phase distribution.

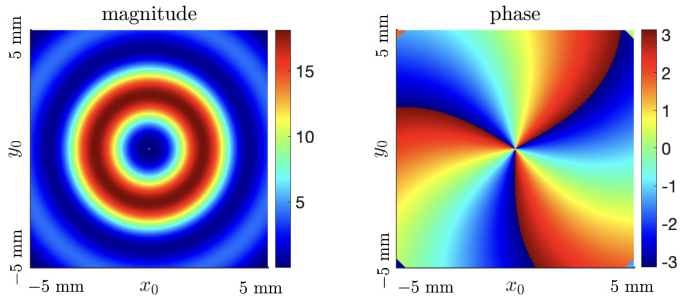

Figure 12: The magnitude (left) and phase (right) of the Fresnel analytical solution in the focal plane for $l = 3$ are shown above. Comments regarding figure (10) apply.

5 Finite Element Model

In sections (2), (3), and (4), the phase plate is assumed to be infinitesimally thin. In practice, the phase plate's varying thickness imparts phase to the incident pressure wave. To investigate this vortex-generation mechanism in more detail, an FEM is constructed in COMSOL according to the dimensions presented in [2].

The phase plate modeled in COMSOL simulation is shown in figures (13) and (14). Since the 3D FEM computation is very time consuming, a lower ka corresponding to a drive frequency of 20 kHz is used, and the transducer is not focused. The phase plate is discretized into 12 equal-area sectors, each with a phase delay of $l\frac{n\pi}{6}$ for $\frac{(n-1)\pi}{6} < \varphi \leqslant \frac{n\pi}{6}$, where $n = 1, 2, \ldots 12$, and where $l = 3$. To minimize reflection, the material properties ρ_1 and c_1 of the phase plate are impedance-matched, i.e., $\rho_1 c_1 = \rho_0 c_0$.

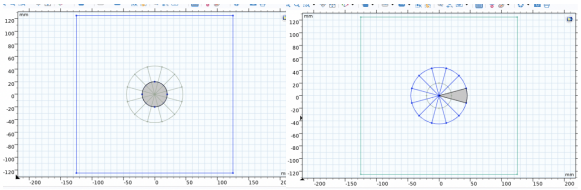

Figure 13: Top view of phase plate (left); single partition (right)

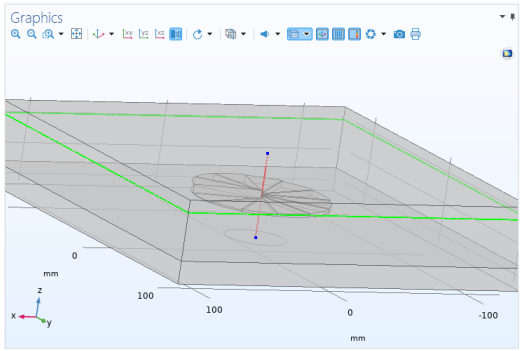

Figure 14: 3D illustration of the setup

Figure (15) is the result of measuring the phase of the FEM a short distance beyond the phase plate. The phase distribution near the axis reveals the $l = 3$ vorticity pattern, validating the vortex-generation mechanism proposed in [2].

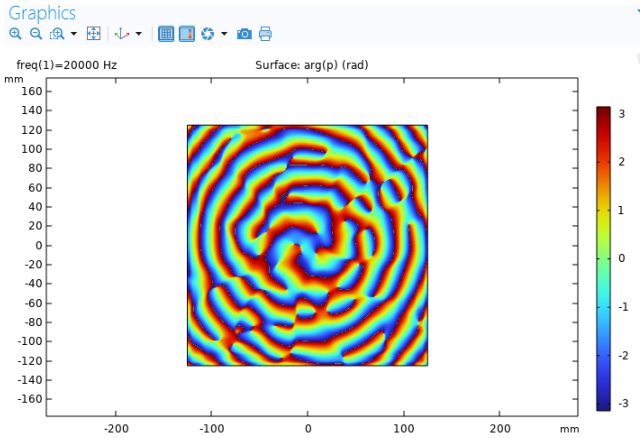

Figure 15: Phase distribution showing the $l = 3$ vorticity

6 Applications

Currently, most vortex beam studies employ brute-force numerical methods, as presented in section (2). These methods provide no insight on the field structure in the vicinity of focal the plane and the dependence on distance from the source. As a result, the stability of the null and the magnitude of the surrounding maximum are unknowns in experiments and engineering applications, necessitating fine-tuning after these devices have been built. For example, Terzi et al. attempt to demonstrate the utility of the $l = 3$ vortex beam by rotating a foam plastic ball floating on water, but the ball "escaped the focal region if the distance between the transducer and the ball was changed even slightly" [2].

The results presented in this work—specifically the Fourier acoustics approach presented in (3) and the analytical solution presented in (4)—address the deficiencies in the theory that would eliminate the need of such fine-tuning. The stability can be improved by taking the gradient of the three-dimensional field in the vicinity of the focal plane numerically in (3) or analytically in 3, giving the local momentum field in that region. The pressure should be chosen such that the magnitude of its gradient is proportional to the object's mass, and such that the null width is on the order of the object's width.

Preliminary results shows that the null width and magnitude both depend on the vorticity; this dependence will be analyzed in the near future to obtain a scaling law. To

achieve precise manipulation of objects, a particular combination of null width and pressure magnitude, and hence a particular vorticity, should be chosen.

Another application of vortex beams is in underwater communication. Since the phase of vortex beams can be uniquely produced, they show promise in underwater communication for their unique angular momentum "fingerprint." As discussed in [9], information can be encoded onto different orbital numbers l of the vortex beam to be received and decoded by an array of transducers. The recovery of the data shows the feasibility of communication using vortex beams at a reduced bit error rate. In this vein, Shi et al. [10] demonstrated a higher spectral density in underwater acoustics communication by multiplexing the orbital angular momentum of the vortex beam, achieving an order-of-magnitude enhancement of data transmission at a single frequency for $l = -4, -3, \ldots 3, 4$. The proposed scaling law that relates vorticity to null width and pressure magnitude may inform transduction and signal-processing aspects of such work.

Conclusion

Inspired by [2], the pressure field of a vortex beam generated by a single-element transducer and phase plate was studied using the Rayleigh integral, Fourier acoustics, the Fresnel limit, and an FEM model. Each mode of study offers unique insights into the formation and structure of vortex beams. The analytical results constitute an extension of the existing literature. To illustrate the value of these findings, a qualitative discussion of the applications of vortex beams was included.

Acknowledgements

C.G. and Y.M. thank Dr. Hamilton for showing them how to incorporate the focusing into the vortex beam, for providing his robust Fourier acoustics code, and for suggesting the change-of-variable required to integrate equation (4).

Author Contributions

C.G. and Y.M. worked together to obtain the Rayleigh solution. Both typed the supplementary notes, and both contributed their respective sections to the report and presentation. C.G. evaluated the Fresnel limit and sought analytical solutions for the pressure amplitude and phase distributions. Y.M. found the FEM and Fourier solutions. Y.M. researched the applications of the vortex beam and its relation to the larger field of ultrasonics.

References

[1] Papathanassiou, E.O. Spiral. *RCA*. Vinyl. (1977).

[2] Terzi, M. E., Tsysar, S. A., Yuldashev, P. V., Karzova, M. M., and Sapozhnikov, O. A. Generation of a vortex ultrasonic beam with a phase plate with an angular dependence of the thickness. *Moscow University Physics Bulletin*. **72**, 61–67 (2017).

[3] See Supplemental Notes, Section 4, for how z_{T} is defined.

[4] See Supplemental Notes, Section 2, for a derivation of the first Rayleigh integral.

[5] See Supplemental Notes, Section 3, for a derivation of the second Rayleigh integral.

[6] Bessel's Integrals. Bessel function. *Wikipedia*.

[7] See Supplemental Notes, Section 6, for an explanation of the Fourier acoustics solution.

[8] Hamilton, M.F., Fourier Acoustics Code. The University of Texas at Austin. (2022).

[9] X. Li, Y. Li, Q. Ma, G. Guo, J. Tu, and D. Zhang, J. Appl. Phys. 127, 124902 (2020).

[10] C. Shi, M. Dubois, Y. Wang, X. Zhang High-speed acoustic communication by multiplexing orbital angular momentum P. Natl. Acad. Sci., 114 (28) (2017), pp. 7250-7253

[11] See Supplemental Notes, Section 7, where this integral representation of the Bessel function is shown. The index n is used in place of l.

[12] Gradshteyn, I.S., Ryzhik, I.M., Qiu, T., and Fischer, P. Table of Integrals, Series and Products. *Academic Press*. 6th ed. (2000).

[13] Bessel's Integrals. Bessel function. *Wikipedia*.